ACS APPLIED MATERIALS & INTERFACES

Research Article

www.acsami.org

# One-Step Calcination-Free Synthesis of Multicomponent Spinel Assembled Microspheres for High-Performance Anodes of Li-Ion Batteries: A Case Study of $MnCo_2O_4$

Chaochao Fu,[†] Guangshe Li,[‡] Dong Luo,[†] Xinsong Huang,[‡] Jing Zheng,[†] and Liping Li*[,†]

[†]Key Lab of Optoelectronic Materials Chemistry and Physics, Fujian Institute of Research on the Structure of Matter, University of Chinese Academy of Sciences, Fuzhou 350002, P. R. China

[‡]State Key Laboratory of Structural Chemistry, Fujian Institute of Research on the Structure of Matter, University of Chinese Academy of Sciences, Fuzhou 350002, P. R. China

Supporting Information

**ABSTRACT:** Multicomponent spinel metal-oxide assembled mesoporous microspheres, promising anode materials for Li-ion batteries with superior electrochemical performance, are usually obtained using different kinds of precursors followed by high-temperature post-treatments. Nevertheless, high-temperature calcinations often cause primary particles to aggregate and coarsen, which may damage the assembled microsphere architectures, leading to deterioration of electrochemical performance. In this work, binary spinel metal-oxide assembled mesoporous microspheres $MnCo_2O_4$ were fabricated by one-step low-temperature solvothermal method through handily utilizing the redox reaction of nitrate and ethanol. This preparation method is calcination-free, and the resulting $MnCo_2O_4$ microspheres were surprisingly assembled by nanoparticles and nanosheets. Two kinds of $MnCo_2O_4$ crystal nucleus with different exposed facet of $(\bar{1}10)$ and $(1\bar{1}2)$ could be responsible for the formation of particle-assembled and sheet-assembled microspheres, respectively. Profiting from the self-assembly structure with mesoporous features, $MnCo_2O_4$ microspheres delivered a high reversible capacity up to 722 mAh/g after 25 cycles at a current density of 200 mA/g and capacities up to 553 and 320 mAh/g after 200 cycles at a higher current density of 400 and 900 mA/g, respectively. Even at an extremely high current density of 2700 mA/g, the electrode still delivered a capacity of 403 mAh/g after cycling with the stepwise increase of current densities. The preparation method reported herein may provide hints for obtaining various advanced multicomponent spinel metal-oxide assembled microspheres such as $CoMn_2O_4$, $ZnMn_2O_4$, $ZnCo_2O_4$, and so on, for high-performance energy storage and conversion devices.

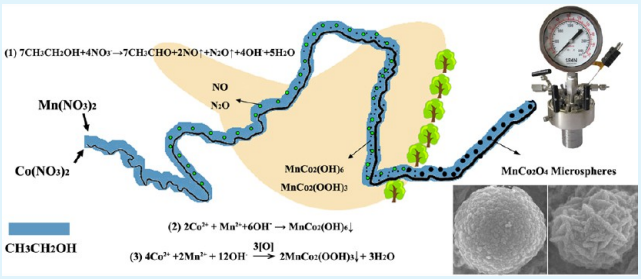


**KEYWORDS:** *$MnCo_2O_4$, microspheres, multicomponent spinel, calcination-free, anode, Li-ion battery*

## 1. INTRODUCTION

Spinel metal-oxide mesoporous microspheres, assembled by nanoscale building blocks (such as nanoparticles,[1,2] nanosheets,[3,4] nanorods,[5,6] nanowires,[7−9] and so on) have been demonstrated to exhibit good electrochemical performance when used in energy storage applications. This is because of the high surface-to-volume ratios, shortened diffusion length between electrolyte and electrode for $Li^+$ insertion/extraction, and the interspaces existing for buffering the pronounced volume variations (>200%) upon the repetitive Li-ion insertion/extraction process in comparison with their bulk counterparts.[10−14] Among these spinel oxide materials, $Co_3O_4$ has been widely investigated as anode of Li-ion batteries, since it can be easily prepared by various synthetic strategies (e.g., low-temperature molten salt method[15,16] and solvothermal method[3]) and since it has a high theoretical capacity of 890 mAh/g (relative to that of 372 mAh/g for graphite) that expects to meet the requirements for storage and utilization of clean energy. However, there still exists an immense demerit for $Co_3O_4$, pertinent to the use of expensive and toxic element, cobalt. Hence, low-cobalt series, based on spinel $AB_2O_4$ binary metal oxides like $ACo_2O_4$ (A = Mn, Ni, Cu, and Zn),[17−22] $AMn_2O_4$ (A = Co, Zn),[23−25] and $AFe_2O_4$ (Co, Ni, Zn)[26−28] are regarded as the more promising candidates due to their relatively low cost and environmental benignity.

Up to date, there have been some great achievements in preparation of spinel binary metal-oxides $AB_2O_4$ with mesoporous assembled microsphere architectures. For example, mesoporous particle-assembled microspheres $MnCo_2O_4$ have been prepared by decomposing a precursor of $Mn_{0.33}Co_{0.67}CO_3$ at 600 °C in air.[17] When zinc−cobalt citrate hollow microspheres were used as the precursors, calcinations at 500

Received: November 1, 2013
Accepted: January 28, 2014
Published: February 6, 2014

   dx.doi.org/10.1021/am404862v | ACS Appl. Mater. Interfaces 2014, 6, 2439−2449

°C led to the mesoporous double-shelled microspheres $ZnCo_2O_4$.[22] Also, 600 °C calcination treatment in air over cobalt and manganese alkoxide precursors leads to $CoMn_2O_4$ mesoporous nanosheet-assembled microspheres.[23] Despite these successes, the preparations of multicomponent spinel oxide anodes are still challenging, since the current preparation methods are mostly based on precursors (e.g., metal hydroxides, oxalates, carbonates, citrates, or alkoxides) that usually require multiple steps and high temperature (>500 °C) post-treatment for formation of final oxides. As a result, several problems that are unbeneficial for the improvement of electrochemical performance and further for the practical applications could be raised: First, two or multiple-step methods are tedious and unhandy. Second, high temperatures often cause primary particles to aggregate and coarsen, which would lead to increase in the diffusion length of $Li^+$ ions. Moreover, the assembled microsphere architectures may be fragile and very easy to be damaged at high temperatures. In addition, high-temperature sintering is not suitable for cost-effective large-scale production. Therefore, it is necessary to develop a new one-step calcination-free method for preparing mesoporous microspheres of multicomponent spinel oxides.

Solvothermal method has shown several advantages like low temperature, constant pressure, and solution environment, by which many materials with very few defects, high crystallinity, and integrity could be obtained. For example, $Mn_3O_4$ has been prepared by one-step solvothermal method, in which $KMnO_4$ is reduced by primary alcohols.[29] $Mn_2O_3$ was also directly synthesized utilizing a solvothermal method.[30] Zhang et al. successfully prepared $Co_3O_4$ nanoparticles in one step using ammonia and cobalt acetate as the starting materials in the mixed solvents of ethanol and water.[31] Therefore, it is most likely that multicomponent spinel metal oxides $MnCo_2O_4$ could be synthesized by one-step solvothermal method.

Herein, we designed a more facile and energy-saving one-step solvothermal method for preparation of mesoporous $MnCo_2O_4$ assembled microspheres. The detailed chemical reactions in this synthesis were systematically investigated by comparing UV−vis absorption spectra of solutions before and after reactions and by detecting the gases released from reactions through mass spectrum analyzer, which are effective to provide more objective understanding and analysis of the reaction processes. When evaluated as an anode material for Li-ion batteries, mesoporous assembled microspheres $MnCo_2O_4$ exhibited an excellent electrochemical performance, indicating a great potential for uses as anode materials of Li-ion batteries. It is worth noting that this preparation method has a universality and could be extended to the syntheses of other multicomponent spinel metal-oxide assembled architectures such as $CoMn_2O_4$, $ZnMn_2O_4$, or $ZnCo_2O_4$ by simple replacement of the raw materials.

## 2. EXPERIMENTAL SECTION

**2.1. Sample Preparation.** In a typical synthesis, the reaction procedure for formation of $MnCo_2O_4$ microspheres could be described as follows: 1 mmol of $Mn(NO_3)_2$ (50 wt % water solution) and 2 mmol of $Co(NO_3)_2{\cdot}6H_2O$ were dissolved into 15 mL of ethanol at room temperature to form a clear red solution. Then, this transparent solution was transferred to a 20 mL autoclave, which was allowed to react at 140 °C for 24 h. The final black products were collected and washed with deionized water and absolute ethanol several times, followed by drying at 80 °C for 8 h in air.

**2.2. Materials Characterization.** Phase structures of the samples were characterized by powder X-ray diffraction (XRD) (Cu K$\alpha$, $\lambda$ = 1.5418 Å) on a Rigaku Miniflex apparatus. The morphology of the samples was observed by field-emission scanning electron microscopy (SEM) (JEOL, Model JEM-2010) and transmission electron microscopy (TEM) (JEOL, Model JEM-2010). The compositions of the samples were analyzed by energy-dispersive X-ray spectroscopy (EDS) attached to SEM instrument and inductive coupled plasma atomic emission spectrometry (ICP-AES). The valence states of Mn and Co ions were examined by electron paramagnetic resonance (EPR) spectroscopy on a Bruker ELEXSYS E500 spectrometer and X-ray photoelectron spectroscopy (XPS) recorded on ESCA-LAB MKII apparatus with a monochromatic Al K$\alpha$ X-ray source. Brynauer-Emmett-Teller (BET) surface area, pore size, and porosity of as-prepared sample were measured by nitrogen adsorption isotherms at 77 K on a Micromeritics ASAP 2000 analyzer.

**2.3. Electrochemical Measurements.** The electrochemical behaviors of the samples were examined using CR-2025-type coin cell. The working electrodes were prepared by mixing the samples ($MnCo_2O_4$ assembled microspheres), carbon black (Super-P @ Li), and binder (polyvinylidene fluoride (PVDF)) at a weight ratio of 5:3:2 and coating on Cu foil. The content of the active materials in each electrode is about 2 mg. The cells were assembled in an argon-filled glovebox ($H_2O$ and $O_2$ < 1 ppm) using lithium foil as the anode, a polymer separator (Celgard 2500), and 1 M $LiPF_6$ in EC:EMC:DMC (1:1:1 in volume) as the electrolyte. The cells were charged and discharged galvanostatically at different current density using a battery cycler (Land Battery Test System) in the voltage range of 0.01 and 3 V at room temperature. Cyclic voltammetry (CV) and electrochemical impedance spectroscopy (EIS) were measured using an electrochemical workstation (CHI660C).

## 3. RESULTS AND DISCUSSION

**3.1. Characterization of Assembled Microspheres $MnCo_2O_4$.** Assembled microspheres $MnCo_2O_4$ were synthesized through a one-step solvothermal method at 140 °C for 24 h. Phase purity and structure of the as-prepared samples were determined by XRD. As indicated in Figure 1a, all diffraction peaks can be indexed according to the standard data for $MnCo_2O_4$ (cubic, lattice parameter $a$ = 8.269 Å, space group $Fd\bar{3}m$ (227), JCPDS card no. 23-1237), which suggests the formation of pure spinel structure. The mean crystallite sizes of the as-synthesized spinel $MnCo_2O_4$ powders, calculated from diffraction lines (220) and (400) using Scherrer formula,[32] were 13.4 and 10.6 nm, respectively. According to the standard cif-file for $(Co_{0.667}Mn_{0.333})^{2+}(Co_{0.667}Mn_{0.333})_2^{3+}O_4$, manganese and cobalt ions in $MnCo_2O_4$ spinel structure are both in mixed valences of +2 and +3, in which $Mn^{2+}$ and $Co^{2+}$ are distributed over tetrahedral stacking interstices, while $Mn^{3+}$ and $Co^{3+}$ occupy the octahedral sites, as illustrated in Figure 1b.

Morphology and chemical composition of $MnCo_2O_4$ sample were investigated by field-emission scanning electron microscopy (SEM) and ICP. As shown in Figure 2a, the sample as-prepared at 140 °C for 24 h were composed of microspheres with size distributed in a range from 1 to 4 $\mu$m. High-magnification SEM images in Figure 2b−d showed that there appeared to be two kinds of microspheres, particle-assembled microspheres, and sheet-assembled microspheres for the sample as-prepared at 140 °C for 24 h. The analysis results of EDS and ICP were displayed in Figure 2e. It is seen that the sample contained metal elements, Mn and Co, only. The elemental compositions of the samples synthesized at 140 °C for 1, 8, and 24 h were determined to be $Mn_{0.96}Co_2O_4$, $Mn_{0.99}Co_2O_4$, and $Mn_{0.97}Co_2O_4$, respectively, very close to the initial ones, which further indicated the formation of pure $MnCo_2O_4$. The preparation method reported here has been successfully extended to other multicomponent spinel metal oxides including yolk-shelled microspheres $CoMn_2O_4$, as-

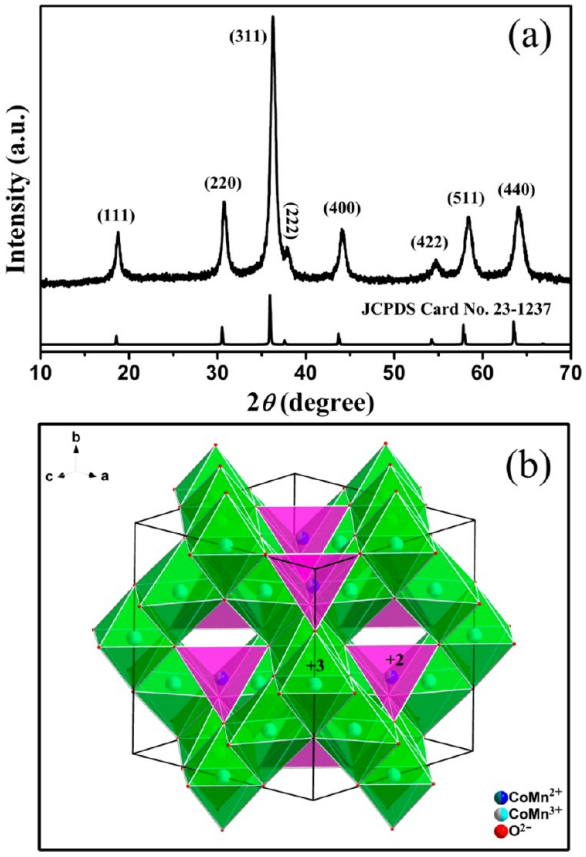


**Figure 1.** (a) XRD patterns and (b) structure illustration of $MnCo_2O_4$ microspheres obtained at 140 °C for 24 h.

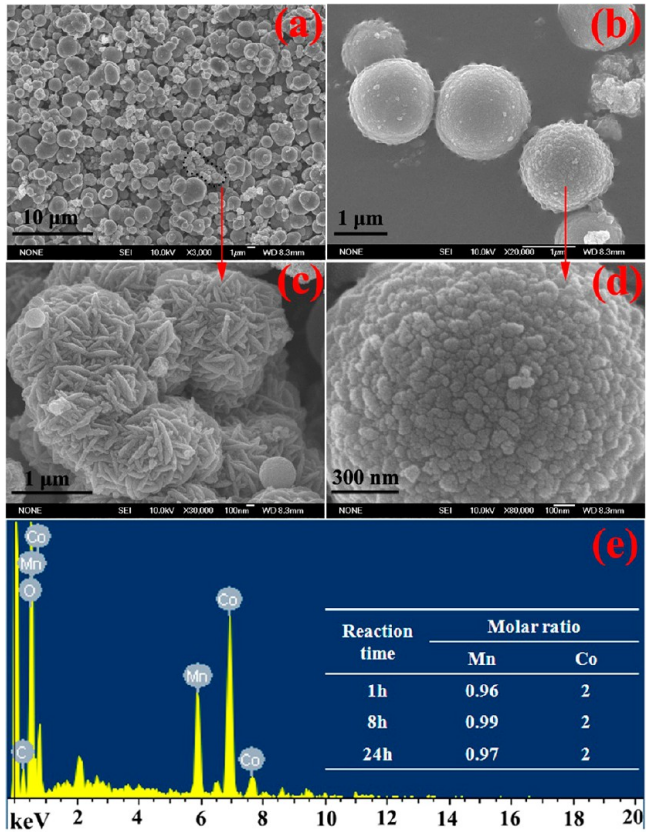


**Figure 2.** (a) Low-magnification, (b–d) high-magnification SEM images, and (e) EDS spectrum of $MnCo_2O_4$ microspheres prepared at 140 °C for 24 h. (inset) Molar ratios of metal ions determined by ICP for $MnCo_2O_4$ microspheres prepared at different reaction times.

sembled microspheres $ZnMn_2O_4$, and hemispheres $ZnCo_2O_4$, as illustrated by XRD and SEM in Supporting Information Figures S1–S3. These results demonstrate the universality of this synthetic method for preparation of multicomponent spinel metal-oxide assembled structures.

The more detailed morphological and structural features of the sample as-prepared at 140 °C for 24 h, which was consisted of particle-assembled microspheres and sheet-assembled microspheres, were further studied by TEM, as indicated in Figure 3. In terms of particle-assembled microsphere as shown in Figure 3a, it was solid with a diameter >1 $\mu$m. A further high-resolution TEM image of the rectangular region in Figure 3b was shown in Figure 3c. High-resolved lattice fringes and corresponding Fourier transform image for the chosen region (i) in Figure 3c indicate the appearance of two groups of vertical crystal planes with lattice spacings of 2.9 and 4.1 Å, which correspond to the planes (220) and (002), respectively. In addition, several sets of visible lattice fringes were observed by Fourier transform image, which could be assigned to the planes (002), (111), (220), and(11$\bar{1}$), respectively (the incident beam parallel to crystal orientation of [$\bar{1}$10], namely, the exposed face is the ($\bar{1}$10) plane). Standing in the sheet-assembled microsphere as indicated in Figure 3e, it was not hollow one either, but in a flowerlike shape. There are a lot of defects in the sheet, as indicated by the magnified TEM image (Figure 3f), high-resolution TEM (Figure 3g), and the corresponding Fourier transform images (Figure 3h). For the latter case, regions ii and iii have shown the consecutive lattice fringes with uniform Fourier transform images. Two groups of crystal planes with an angle of 31.5°were observed, showing lattice spacings of 2.5 and 2.9 Å that correspond to the planes (311) and (220), respectively. Moreover, both sets of lattice fringes of regions ii and iii could be ascribed to the planes (220), (311), and (1$\bar{1}$1), respectively (the incident beam was parallel to[1$\bar{1}$2]; that is, the exposed face was the (1$\bar{1}$2) plane).

The oxidation states of metal ions in the sample as-prepared at 140 °C for 24 h were further investigated by XPS, as indicated in Figure 4. All binding energies were calibrated for specimen charging by referencing the C 1s peak at 284.6 eV. In Co2p spectrum (Figure 4a), two major signals were observed located at 780.4 and 795.7 eV with weak shakeup satellite peaks at 788 and 802 eV. The spin–orbit splitting was ca. 15 eV. Therefore, both signals could be attributed to Co $2p_{3/2}$ and Co $2p_{1/2}$ levels, respectively. It is well-established that the Co $2p_{3/2}$ level of $Co^{3+}$ ions in metal oxides usually locates at 779.6 eV with its satellite peak at 790 eV, showing a binding energy difference of about 10 eV.[33−35] For $Co^{2+}$ ions like those in CoO,[36,37] the Co $2p_{3/2}$ level is approaching to 780.5 eV with its satellite peak at about 786 eV. Comparatively, for typical $Co_3O_4$ with mixed valence state of $Co^{3+}$ and $Co^{2+}$, the binding energies of Co $2p_{3/2}$ and Co $2p_{1/2}$ are in the ranges of 779.5–780.3 and 795.0–795.9 eV, respectively, with satellites occurring about 7–9 eV higher in binding energy from the main signals.[38,39] Therefore, based on the peak widths of the signals Co $2p_{3/2}$ and Co $2p_{1/2}$ and on the distance of satellite apart from Co $2p_{3/2}$ levels, it is most likely that there coexist $Co^{2+}$ and $Co^{3+}$ for the present samples. Accordingly, the Co 2p levels could be deconvoluted into two sets of quartets (Co $2p_{3/2}$ and $2p_{1/2}$ and their corresponding satellites) with the restrictions: the spin–


dx.doi.org/10.1021/am404862v | ACS Appl. Mater. Interfaces 2014, 6, 2439–2449

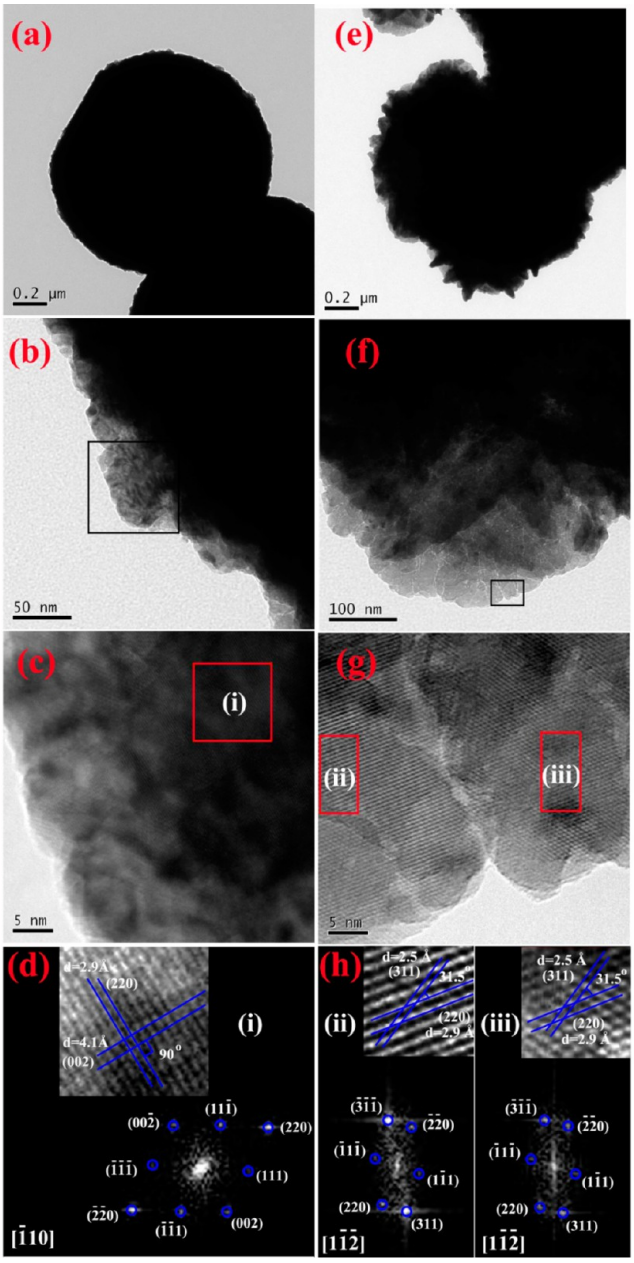


**Figure 3.** (a, b) TEM images, (c) HRTEM image of rectangular region in part b, and (d) high-resolved lattice fringes and Fourier transform image taken by HRTEM in regions (i) of particle-assembled $MnCo_2O_4$ microspheres. (e, f) TEM images, (g) HRTEM image of rectangular region in part f, and (h) high-resolved lattice fringes and Fourier transform images taken by HRTEM in regions ii and iii of sheet-assembled $MnCo_2O_4$ microspheres.

orbital splitting of Co $2p_{3/2}$ and Co $2p_{1/2}$ is about 15 eV, and the intensity ratio of Co $2p_{3/2}$ to Co $2p_{1/2}$ is fixed at 2. Data analyses showed that about 56.2% of cobalt was in the valence state of $Co^{3+}$. Similarly, for Mn 2p core level (Figure 4b), two main peaks of Mn $2p_{3/2}$ at 642.0 eV and Mn $2p_{1/2}$ at 653.7 eV could be divided into four subpeaks: two at 641.6 and 653.3 eV are assigned to the binding energy of $Mn^{2+}$, while other two at 643.4 and 654.2 eV are attributed to the existence of $Mn^{3+}$.[17,40] The molar ratio of $Mn^{2+}$ to $Mn^{3+}$ was thus calculated to be 1.6.

The presence of $Mn^{2+}$ in the sample as-prepared at 140 °C for 24 h was further confirmed by EPR data measured at room temperature (Figure 5), where an intrinsic signal for $Mn^{2+}$ that

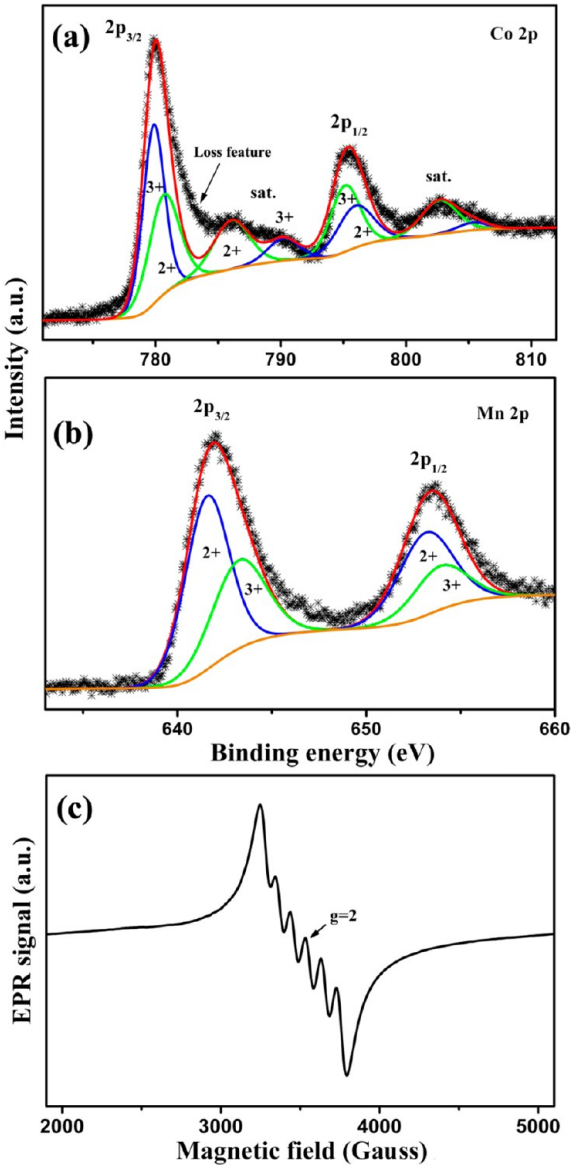


**Figure 4.** XPS spectra for levels (a) Co 2p and (b) Mn 2p, as well as (c) EPR spectrum measured at room temperature for $MnCo_2O_4$ microspheres as-prepared at 140 °C for 24 h.

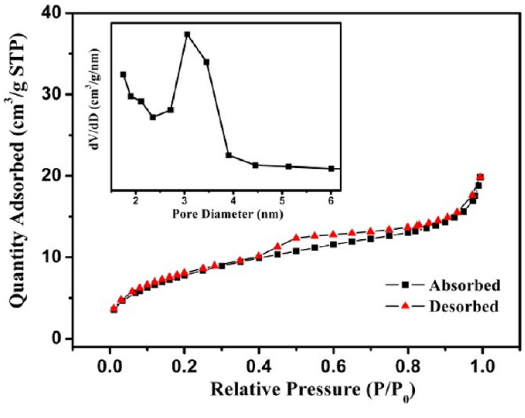


**Figure 5.** Nitrogen adsorption−desorption isotherm and the corresponding pore size distribution (inset) of $MnCo_2O_4$ microspheres.


dx.doi.org/10.1021/am404862v | ACS Appl. Mater. Interfaces 2014, 6, 2439−2449

contains a wide resonance at $g$ = 2.00 with six resolved hyperfine lines[41] was clearly seen. Therefore, $Co^{2+}$/ $Co^{3+}$ and $Mn^{2+}$/ $Mn^{3+}$ coexist in $MnCo_2O_4$ microspheres that were prepared by the present solvothermal method.

Specific surface areas of the $MnCo_2O_4$ microspheres as-prepared at 140 °C for 24 h were characterized by BET using nitrogen adsorption isotherm, as shown in Figure 5. The isotherm of $MnCo_2O_4$ microspheres can be classified as type-IV with a type-H4 hysteresis loop, indicating a mesoporous structure.[42] According to the corresponding Barrett−Joyner−Halenda (BJH) plots (the inset of Figure 5) recorded from nitrogen isotherms, the average pore size for $MnCo_2O_4$ microspheres was about 3 nm, characteristic of mesoporous materials. In addition, BET surface areas of $MnCo_2O_4$ microspheres were 29.1 $m^2/g$, which is much bigger than that of 18.0 $m^2/g$ reported by Xiong and co-workers who used a two-step method.[17] Relatively large surface area is beneficial for the contact with the electrolyte that possibly results in a considerable improvement in the electrochemical properties.

**3.2. Possible Formation Mechanism of $MnCo_2O_4$ Assembled Microspheres.** *3.2.1. Chemical Reactions in Solvothermal Process.* As described above, $MnCo_2O_4$ microspheres were successfully prepared by one-step solvothermal method using $M(NO_3)_2$ (M = Mn, Co) and ethanol as raw materials. Here, choosing nitrates of transition metals as the starting materials is crucial for the formation of $MnCo_2O_4$ assembled microspheres $MnCo_2O_4$. To stress this, standard electrode potentials for ethanol and nitrate should be determined. The standard electrode potential for ethanol when oxidized into aldehyde is −0.197 V, while that of nitrate ($NO_3^-$) is about 0.4 V ($\varphi_{NO_2^-/NO_3^-}$ = 0.421 V, $\varphi_{NH_4^+/NO_3^-}$ = 0.36 V).[43−45] Therefore, nitrate has enough ability to oxidize ethanol into aldehyde at special conditions, which would impose some impacts on the formation of $MnCo_2O_4$ microspheres. In order to understand the roles of nitrate ($NO_3^-$), we performed a series of control experiments. Figure 6 showed the variations of UV−visible spectra of the solutions before and after reactions in the series of control experiments. When $MCl_2$ (M = Mn, Co) replaced $M(NO_3)_2$ (M = Mn, Co) to serve as the reactants, no products were obtained. Moreover, the prereaction and residual solutions gave the exact same spectra (Figure 6), which suggest no reaction occurred. When $Mn(NO_3)_2$ or $Co(NO_3)_2$ was used alone as the reactants, the UV−visual absorption spectra for the prereaction and residual solutions were obviously changed, similar to the cases when both of $Mn(NO_3)_2$ and $Co(NO_3)_2$ were used as the reactants. Before the reaction (Figure 6a), a broad peak associated with the presence of $NO_3^-$ species was observed at 250−350 nm,[43,44] which however disappeared after the reaction. Another broad peak that characterized the d−d transition of $Co^{2+}$ was observed at 450−600 nm, which also disappeared after the reaction, indicating the complete precipitation of Co ions. After the reaction (Figure 6b), a set of zigzagged peaks in the range from 300 to 400 nm appeared, which were associated with the presence of certain new organic species that were derived from the reactions between ethanol and $NO_3^-$.[44] In conclusion, nitrates play a vital role in driving the reactions for the formation of $MnCo_2O_4$ microspheres.

Mass spectra analyses of the gases released during the reaction were conducted to further comprehend the redox reactions between ethanol and $NO_3^-$. The inset of Figure 7 shows the gas export device. The gases were exported from the

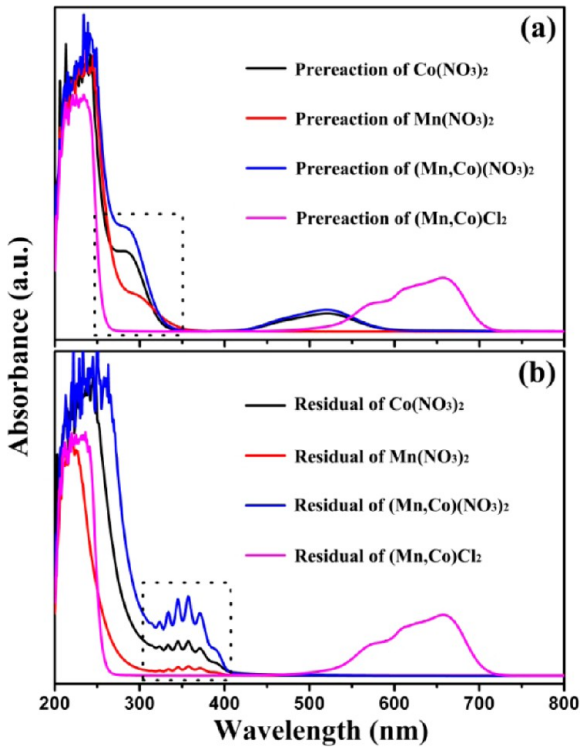


**Figure 6.** UV−visible spectra of (a) prereaction solution and (b) residual solution after formation reaction at 140 °C. All absorption spectra were recorded by taking ethanol as the reference.

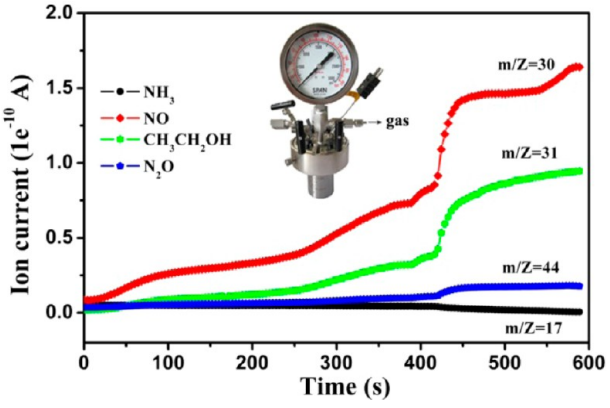


**Figure 7.** Mass spectra of gases released from solvothermal reaction process. (inset) Gas export device (Parr 4791 Nonstirred Reactor).

reactor at 80 °C. From the viewpoint of inorganic chemistry, the redox reaction of nitrate could give rise to either nitric oxides (i.e., NO, $NO_2$, and $N_2O$) or ammonia gas ($NH_3$).[46] The possibility of $NO_2$ gas can be ruled out because the exported gas was colorless. As Figure 7 shows, three signals with mass-charge ratios of $m/Z$ of 30, 31, and 44 were detected in mass spectrum. These signals could be assigned to NO ($m/Z$ = 30), $CH_3CH_2OH$ ($m/Z$ = 31), and $N_2O$ ($m/Z$ = 44), respectively. The signal of $m/Z$ = 17 remained at the baseline level, indicating the absence of $NH_3$. In conclusion, NO and $N_2O$ were generated during the redox reaction process between $NO_3^-$ and ethanol. Therefore, the chemical reaction equation could be described as follows:

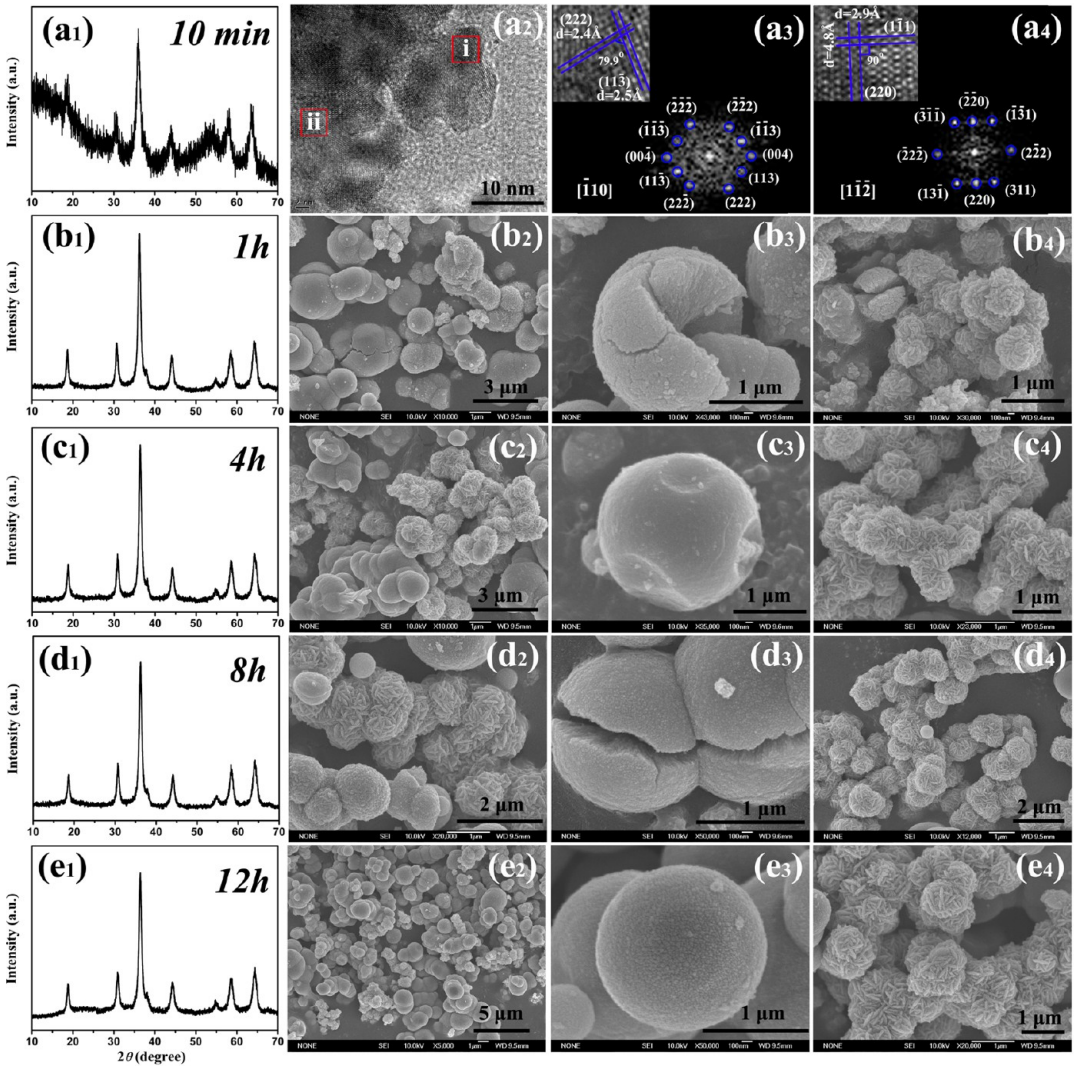


**Figure 8.** XRD patterns, HRTEM, high-resolved lattice fringes, and Fourier transform images taken by HRTEM in regions i and ii (corresponding to $a_3$ and $a_4$, respectively), and SEM images of the as-prepared $MnCo_2O_4$ samples with different treatment times of ($a_1$–$a_4$) 10 min, ($b_1$–$b_4$) 1 h, ($c_1$–$c_4$) 4 h, ($d_1$–$d_4$) 8 h, and ($e_1$–$e_4$) 12 h at 140 °C.

$$7CH_3CH_2OH + 4NO_3^- \rightarrow 7CH_3CHO + 2NO\uparrow + N_2O\uparrow + 4OH^- + 5H_2O \quad (1)$$

Based on eq 1, the subsequent chemical reactions in formation process of $MnCo_2O_4$ microspheres could be

$$2Co^{2+} + Mn^{2+} + 6OH^- \rightarrow MnCo_2(OH)_6\downarrow \quad (2)$$

$$4Co^{2+} + 2Mn^{2+} + 12OH^- \xrightarrow{3[O]} 2MnCo_2(OOH)_3\downarrow + 3H_2O \quad (3)$$

$$MnCo_2(OH)_6 + 4Co^{2+} + 2Mn^{2+} + 12OH^- \xrightarrow{3[O]} 3MnCo_2O_4 + 6H_2O \quad (4)$$

$$2MnCo_2(OOH)_3 + 2Co^{2+} + Mn^{2+} + 6OH^- \rightarrow 3MnCo_2O_4 + 6H_2O \quad (5)$$

Therefore, the formation process of $MnCo_2O_4$ microspheres could be described as follows: First, with the temperature rising, ethanol and nitrate may start to react and to generate $OH^-$, NO, and $N_2O$ bubbles. Second, $Mn^{2+}$ and $Co^{2+}$ could combine with $OH^-$ to form a $MnCo_2(OH)_6$ crystal nucleus. In the meanwhile, $MnCo_2(OOH)_3$ crystal nucleus are also produced in the oxidation environment. Finally, $MnCo_2(OH)_6$ and $MnCo_2(OOH)_3$ further react with $Mn^{2+}$, $Co^{2+}$, and $OH^-$ that gathered around these crystal nucleus and dehydrate at high temperature and pressure to generate $MnCo_2O_4$ crystal nucleus, as shown in eqs 4 and 5. It is worth noting that NO and $N_2O$ bubbles could act as a gas template in forming microspheres.

*3.2.2. Morphology Evolution Process of $MnCo_2O_4$ Assembled Microspheres.* In order to reveal the formation process of the particle-assembled and sheet-assembled microsphere architectures in the sample as-prepared at 140 °C for 24h in more details, time-dependent experiments at 140 °C were carried out, and the resultant products were analyzed by TEM and SEM. The representative TEM and SEM images of the products prepared at certain reaction time intervals are shown in Figure 8.

When the reaction time was 10 min, the obtained sample was $MnCo_2O_4$ at low yield (less than 5%, indicating the $OH^-$ was


dx.doi.org/10.1021/am404862v | ACS Appl. Mater. Interfaces 2014, 6, 2439–2449

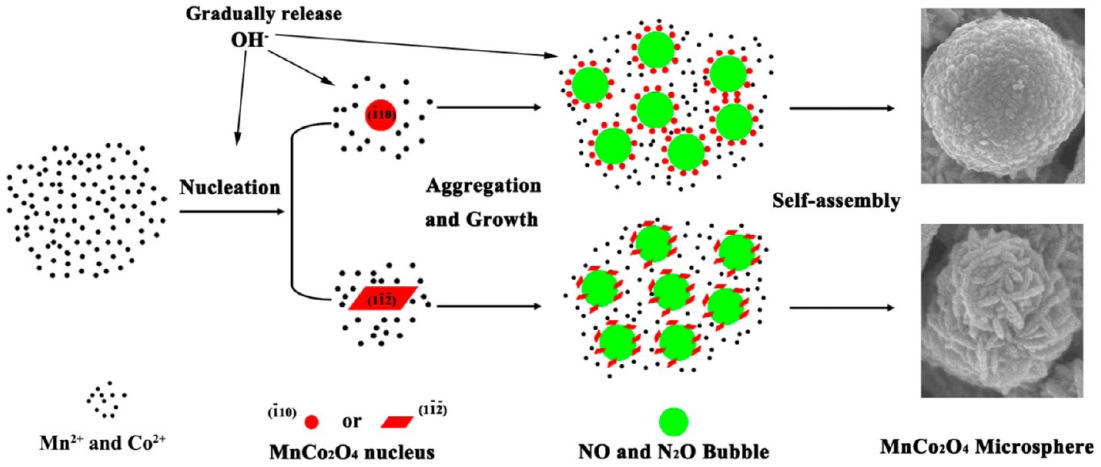


**Figure 9.** Schematic illustration of morphology evolution process of assembled microsphere architectures $MnCo_2O_4$.

gradually released via reaction eq 1), and no assembled microspheres were formed but nanoparticles and nanosheets, as indicated by TEM and HRTEM images in Supporting Information Figure S4 and Figure 8$a_2$−$a_4$. Figure 8$a_3$ shows the high-resolved lattice fringes from region (i) in Figure 8$a_2$. It is seen that the lattice spacings were 2.4 and 2.5 Å, which could be assigned to the planes (222) and (11$\bar{3}$) with an intersection angle of 79.9°, respectively. The corresponding Fourier transform images indicated that the sets of lattice fringes could be ascribed to the planes (222), (113), and (004), respectively, and the incident beam is parallel to crystal orientation of [$\bar{1}$10] (that is, the exposed face was ($\bar{1}$10) plane), which was the same as the case of Figure 3d. Therefore, the corresponding particle was the precursor of particle-assembled microspheres.

The high-resolved lattice fringes from region ii in Figure 8$a_2$ were shown in Figure 8$a_4$. The lattice spacings of two vertical planes were 2.9 and 4.8 Å, which could be ascribed to the planes of (220) and (1$\bar{1}$1), respectively. The corresponding Fourier transform images indicated that the sets of lattice fringes could be ascribed to the planes of (220), (311), and (2$\bar{2}$2), respectively, and the incident beam is parallel to crystal orientation of [1$\bar{1}$2] (that is, the exposed face was (1$\bar{1}$2) plane), which is the same as the case of Figure 3h, Therefore, the corresponding sheet was the precursor of sheet-assembled microsphere.

When the reaction time increased to 1 h, the yield was higher than 90%. The broken particle-assembled microspheres with many cracks are ubiquitous (Figure 8$b_2$ and $b_3$). Comparatively, the sheet-assembled microspheres mainly existed in the form of clusters, and little broken sheet-assembled microspheres were observed after treatment for 1 h (Figure 8$b_4$). When the reaction time was prolonged to 8 h, a small number of broken particle-assembled microspheres with cracks still remained (Figure 8$d_3$). In the meanwhile, the sheet-assembled microspheres have been fully developed (Figure 8$d_4$). When the reaction time was further prolonged to 12 h, similar to that shown in Figure 2, fully developed particle-assembled and sheet-assembled microspheres were observed. These observations demonstrated that nanoparticles with exposed face of ($\bar{1}$10) plane were assembled into particle-assembled microspheres, while nanosheets with exposed face of (1$\bar{1}$2) plane grew and were assembled into sheet-assembled microspheres. The sheet-assembled microsphere architectures grow faster than particle-assembled microsphere architectures. Besides these, the spinel structure of $MnCo_2O_4$ was retained for the whole reaction periods from 10 min to 12 h, as indicated by XRD.

On the basis of these results, the possible formation mechanism for $MnCo_2O_4$ particle-assembled and sheet-assembled microspheres could be proposed, as shown in Figure 9. First, the hydroxyl ($OH^-$) that was gradually released would combine with $Mn^{2+}$ and $Co^{2+}$ to form $MnCo_2(OH)_6$ and $MnCo_2(OOH)_3$ crystal nucleus with nanoparticle or nanosheet-shape as described in reactions 1−3. Then, $Mn^{2+}$, $Co^{2+}$, and $OH^-$ would be adsorbed on the surface of $MnCo_2(OH)_6$ and $MnCo_2(OOH)_3$ crystal nucleus and further precipitated on the surface by reactions 4 and 5. Consequently, small $MnCo_2O_4$ nucleuses with nanoparticle (exposed with facet ($\bar{1}$10)) or nanosheet-shape (exposed with facet (1$\bar{1}$2)) were received, and nanosheets continued to grow and form larger nanosheets. Finally, with the assistance of the NO and $N_2O$ bubbles masterplate, the particles and sheets assembled into particle-assembled and sheet-assembled microspheres. Perhaps because of differences on surface charges between ($\bar{1}$10) and (1$\bar{1}$2) planes, there were no microspheres that were consisted of nanoparticles and cluster of nanosheets together. Since the sheets have bigger surface areas than small particles and can adsorb more $Mn^{2+}$, $Co^{2+}$, and $OH^-$, the sheet-assembled microsphere architectures grew faster than particle-assembled microsphere architectures and thus are primarily present in the form of clusters, while the particle-assembled microsphere architectures mainly existed in the monodisperse form.

**3.3. Electrochemical Performance of $MnCo_2O_4$ Microspheres.** It is well documented that the electrochemical performance of active materials is greatly related to the morphology and assembled structures.[47] Consequently, formation of mesoporous nanoparticle-assembled and nanosheet-assembled microspheres is distinctly important to the electrochemical performance of $MnCo_2O_4$. These hierarchical structures have the merits of efficient contact between the surface of active materials and electrolyte even at high rates. Moreover, the electrodes composed of numerous nanosized crystallites will reduce the diffusion length of $Li^+$ ions and greatly enhance the electrochemical kinetics. On the other hand, the interspace in the mesoporous structures could buffer the volume variations associated with the repeated $Li^+$

insertion/extraction process during cycles, which might greatly improve the cycling capability.

Motivated by these interesting structural features, the electrochemical properties of the $MnCo_2O_4$ microspheres synthesized at 140 °C for 24 h were measured by configuring them as the laboratory-based CR2025 coin cell. Figure 10a shows the first five consecutive cyclic voltammetry (CV) curves of $MnCo_2O_4$ microspheres at a scan rate of 0.1 mV/s in the voltage range of 0.01−3 V. In the first cycle, there was a sharp reduction peak at 0.67 V in the cathodic process, which is assigned to the reduction of $MnCo_2O_4$ to metallic Mn and Co.[7,17,23] Two broad oxidation peaks were observed at 1.49 and 1.98 V in the anodic scan, corresponding to the oxidation of Mn to $Mn^{2+}$ and Co to $Co^{2+}$, respectively.[17,24] The second cycle exhibited two pairs of distinct redox peaks: One at 0.86/1.5 V corresponds to the reduction/oxidation of MnO while another at 1.15/2.02 V is ascribed to the reduction/oxidation of CoO. In the subsequent cycles, reduction/oxidation peaks were similar to that of the second cycle, indicating a good cycle reversibility for the electrochemical reactions. On the basis of the cyclic voltammograms, the entire electrochemical process can be classified as follows:

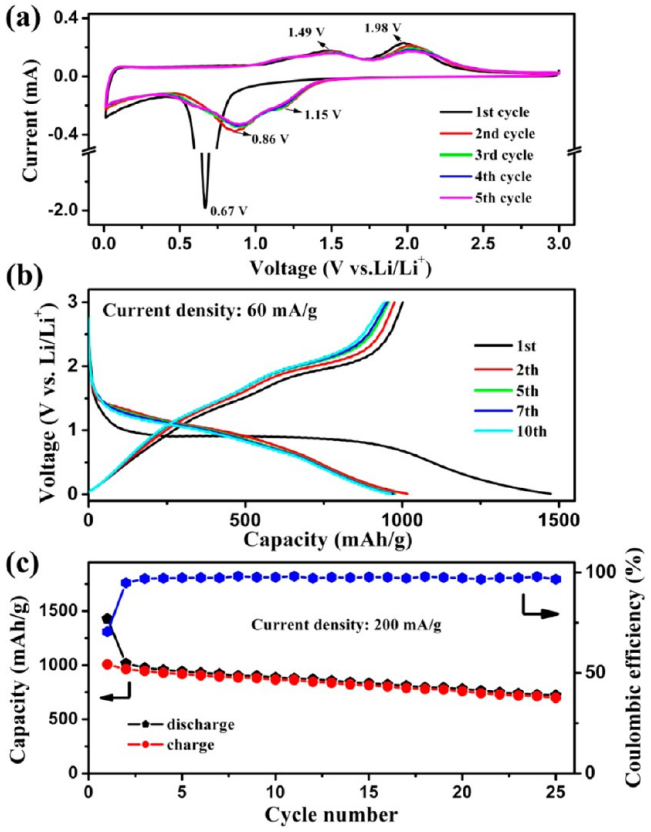


**Figure 10.** (a) First five cyclic voltammetry curves at a scan rate of 0.1 mV $s^{-1}$, (b) galvanostatic discharge−charge profiles for the first ten cycles at a current density of 60 mA/g, and (c) cycling performance of $MnCo_2O_4$ microspheres at a current density of 200 mA/g in the voltage range of 0.01−3 V.

$$MnCo_2O_4 + 8Li^+ + 8e^- \rightarrow Mn + 2Co + 4Li_2O \quad (6)$$

$$Mn + 2Co + 3Li_2O \leftrightarrow MnO + 2CoO + 6Li^+ + 6e^- \quad (7)$$

That is, when $MnCo_2O_4$ microspheres were electrochemically discharged with lithium metal, its crystal structure was destructed, and the nanosized Mn, Co, and $Li_2O$ would form, as shown in eq 6. Subsequently, the follow-up electrochemical process may be on the basis of oxidation/reduction reactions of MnO and CoO, respectively, as shown in eq 7.

Figure 10b showed the galvanostatic discharge−charge curves of different cycles at a current density of 60 mA/g. The cells made from $MnCo_2O_4$ microspheres synthesized at 140 °C for 24 h exhibited the initial discharge and charge capacities of 1473 and 1002 mA h/g, which are higher than the theoretical value (906 mA h/g) based on eq 6. The excess capacities could be associated with the decomposition of the electrolyte at low voltages that generates a solid electrolyte interphase (SEI) layer. The large irreversible capacity loss of the first cycle can be assigned to the crystal structure destruction/amorphization[48−50] or the phenomenon that the formed SEI film cannot be completely decomposed during the first charge.[17,24] After 10 discharge−charge cycles, the discharge capacity and columbic efficiency were still as high as 963 mAh/g and 98%, respectively. When the current density increased to 100 mAh/g, the first two discharge capacities were 1366 and 960 mAh/g, respectively, while the 25th discharge capacity was 737 mAh/g. Clearly, under the condition of low current density, $MnCo_2O_4$ assembled microspheres exhibited a superior electrochemical performance.

Figure 10c exhibited the cycling performance curves at a current density of 200 mA/g in the voltage range of 0.01−3 V. The initial discharge capacity and columbic efficiency were 1430 mAh/g and 70.5%, respectively. After 25 cycles, the discharge specific capacity of $MnCo_2O_4$ microspheres was 722 mAh/g, as good as that of $MnCo_2O_4$ samples prepared by carbonate precursors with subsequent heating treatment methods reported elsewhere.[17] This further confirms that our one-step solvothermal method has the more facile and energy-saving advantages. It is also noted that such a discharge specific capacity after 25 cycles is also larger than the theoretical storage capacity (i.e., 681 mAh/g) based on the eq 7. There are two possible reasons for this discrepancy. The first one may be ascribed to the reversible formation/dissolution of polymeric gel-like film stemmed from electrolyte degradation, which has also been observed in many transition metal oxides.[17,24,51,52] The second one may also be contributed from the mesoporous structures of $MnCo_2O_4$ microspheres with high BET surface areas.

To better understand the electrochemical behaviors of $MnCo_2O_4$ microspheres synthesized at 140 °C for 24 h, we also investigated the cycling performance at higher current densities of 400 and 900 mA/g, as shown in Figure 11a. At a current density of 400 mA/g, the discharge capacity was 553 mAh/g after 200 cycles, which maintained 81.2% of its theoretical capacity (681 mAh/g). There was a slight increase in discharge capacity toward the end of the cycle run, which could be ascribed to the growth of polymer/gel-like film.[27,53] At a higher current density of 900 mA/g, the discharge capacity was 447 mAh/g after 30 cycles, approaching 460 mAh/g after 30 cycles at a current density of 800 mA/g reported in the counterparts prepared previously by a heating post-treatment method.[47] Further prolonged to 200 cycles, the discharge capacity was still as high as 320 mAh/g and the columbic efficiency was 98.7%.

Besides the high specific capacity and good cyclability, the rate performances of $MnCo_2O_4$ microspheres at different

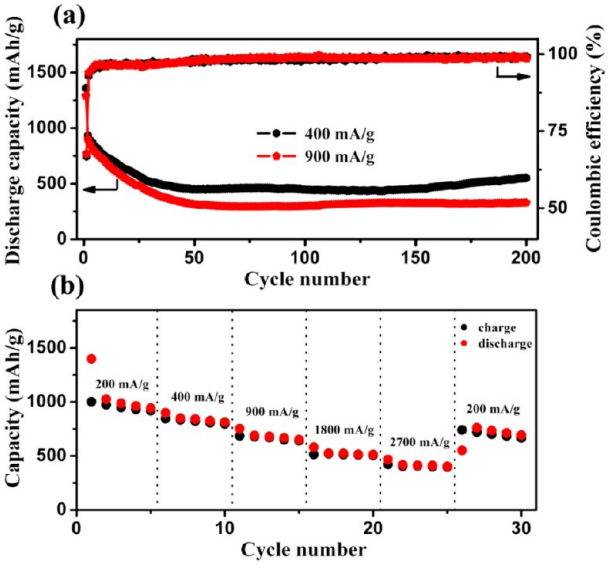


**Figure 11.** (a) Cycling performance and (b) rate capability of $MnCo_2O_4$ microspheres at different current densities in the voltage range of 0.01−3 V.

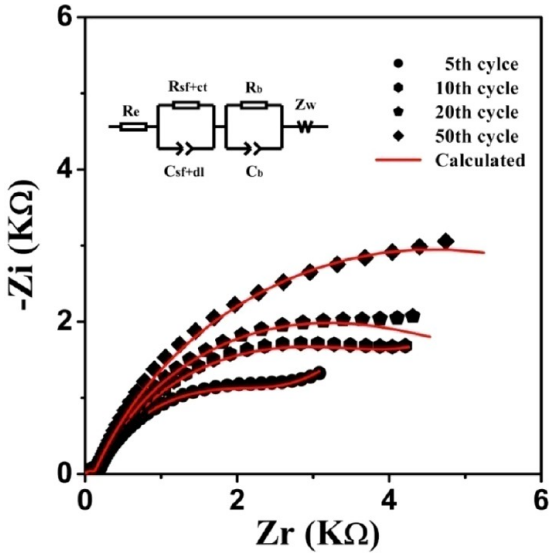


**Figure 12.** Nyquist plots of $MnCo_2O_4$ microspheres after 5, 10, 20, and 50 cycles in the fully charged state at a current density of 400 mA/g in the frequency range from 100 kHz to 0.01 Hz. (inset) Equivalent circuit.

current densities from 200 to 2700 mA/g were also demonstrated as shown in Figure 11b. It can be seen that the discharge capacity was 943 mAh/g after 5 cycles at a current density of 200 mA/g. The current density was subsequently increased stepwise to 400, 900, 1800, and 2700 mA/g, and the corresponding discharge capacities after 5 cycles at each current densities were 814, 652, 513, and 403 mAh/g. When the current density afresh decreased to 200 mA/g, the discharge capacity recovered to 762 mAh/g at 27 cycles. These results demonstrate that $MnCo_2O_4$ microspheres synthesized at 140 °C for 24 h have an excellent rate performance, showing a great potential as high-rate anode materials for Li-ion batteries.

Electrochemical impedance spectroscopy represents an important technique for evaluating interfacial electrochemistry and reaction kinetics in Li-ion battery materials.[54−57] The impedance spectra were measured on the $MnCo_2O_4$/Li cells to further understand the good electrochemical performance of mesoporous microspheres $MnCo_2O_4$. Nyquist plots were obtained in the frequency range from 100 kHz to 0.01 Hz at the fully charged state after 5, 10, 20, and 50 cycles at a current density of 400 mA/g. As shown in Figure 12, the impedance spectra were composed of two semicircles in the high and middle frequency regions and incline lines in the low frequency domains. Analyzed by Zsimpwin software, these impedance data were fitted to the equivalent electrical circuit shown in the inset of Figure 12. Here, $R_e$ represents the internal resistance of the cell. High frequency semicircles can be ascribed to a combination of the surface film resistance and the charge transfer impedance ($R_{sf+ct}$) while $C_{sf+dl}$ is a constant phase element due to the surface film and double layer capacitance. $R_b$ and $C_b$ are bulk resistance and bulk capacitance in the middle frequency region.[48,58,59] $W$ describes the Warburg impedance that is directly related to the solid state diffusion of lithium ion inside the active particles and signified by the straight sloping line in low frequency region. The Warburg impedance is not shown for 10−50th cycles due to the limit of test frequency.

As shown in Figure 12, all Nyquist plots exhibited two semicircles in the high and middle frequency regions. The values of $R_e$, $R_{sf+ct}$, and $R_b$ after different cycles are listed in Table 1. It can be seen that there were no significant changes for the values of $R_{sf+ct}$ from the 5th to 50th cycles, which indicates that SEI films are stable in the cycle process. However, lithium intercalation/deintercalation process became more difficult, as indicated by the significant increase in the values of $R_b$ from 1948 to 8930 Ω with increasing the cycle numbers. As a result, the discharge capacities gradually decreased from 1360 to 453 mAh/g during the initial 50 cycles at a current density of 400 mA/g.

**Table 1. Fitted Parameters for EIS Data Obtained by Zsimpwin Software Using Equivalent Circuit in the Inset of Figure 12**

| cycle number | $R_e$ (Ω) | $R_{sf+ct}$ (Ω) | $CPE_{sf+ct}$ (μF) | $R_b$ (Ω) | $CPE_b$ (mF) |
|---|---|---|---|---|---|
| 5th | 2.29 | 138.6 | 17.6 | 1948 | 0.6 |
| 10th | 2.26 | 145.7 | 20.3 | 3446 | 0.5 |
| 20th | 2.77 | 133.1 | 19.9 | 4651 | 0.6 |
| 50th | 2.40 | 116.5 | 32.2 | 8930 | 0.6 |

It appears that owing to the self-assembly structure with mesoporous features, $MnCo_2O_4$ microspheres showed an excellent electrochemical performance and could have great application potential for energy storage devices.

## 4. CONCLUSIONS

We have designed a more facile and energy-saving calcination-free solvothermal method for preparation of mesoporous assembled-microspheres $MnCo_2O_4$. The mesoporous microspheres $MnCo_2O_4$ were assembled by nanoparticles and nanosheets. The transition metal ions in these assembled microspheres $MnCo_2O_4$ were present in a mixed valence state of +2 and +3. Concerning the formation mechanism of the assembled-microspheres $MnCo_2O_4$, nitrates as the starting materials are very important in driving the chemical reactions. The presence of two kinds of assembled microspheres $MnCo_2O_4$ is closely related to the formation of $MnCo_2O_4$ crystal nucleus with different exposed facet of $(\bar{1}10)$ and $(1\bar{1}2)$ at the beginning of the reaction. When evaluated as anode

materials for Li-ion batteries, the assembled microspheres $MnCo_2O_4$ exhibited a superior electrochemical performance. For instance, the microspheres delivered a high reversible capacity of 722 mAh/g after 25 cycles at a current density of 200 mA/g and capacities up to 553 and 320 mAh/g after 200 cycles at higher current density of 400 and 900 mA/g, respectively. After cycling with various current densities, the electrode could deliver a capacity of 403 mAh/g at an extremely high current density of 2700 mA/g (about 4C, 1C = 681 mAh/g). More importantly, the preparation method reported herein has been successfully extended to synthesize other multicomponent spinel metal-oxides assembled nanostructures, such as yolk-shelled $CoMn_2O_4$ microspheres, assembled microspheres $ZnMn_2O_4$, and hemispheres $ZnCo_2O_4$, which provides a new idea for obtaining various advanced metal-oxide assembled architectures for uses in high-performance energy storage and conversion devices.

## ■ ASSOCIATED CONTENT

### Supporting Information

Preparation process, XRD patterns, SEM images, EDS analysis of the yolk-shelled microspheres $CoMn_2O_4$, assembled microspheres $ZnMn_2O_4$, and hemispheres $ZnCo_2O_4$. This material is available free of charge via the Internet at http://pubs.acs.org.

## ■ AUTHOR INFORMATION

### Corresponding Author

*E-mail: lipingli@fjirsm.ac.cn. Fax: (+) 86-591-83702122.

### Notes

The authors declare no competing financial interest.

## ■ ACKNOWLEDGMENTS

This work was financially supported by NSFC (21271171 and 21025104), National Basic Research Program of China (2011CB935904), and FJPYT (2060203) and FJIRSM fund (SZD08002-3, SZD09003-1, and 2010KL002).

## ■ REFERENCES

(1) Xiong, Q. Q.; Tu, J. P.; Lu, Y.; Chen, J.; Yu, Y. X.; Qiao, Y. Q.; Wang, X. L.; Gu, C. D. *J. Phys. Chem. C* **2012**, *116*, 6495−6502.
(2) Xu, J.-S.; Zhu, Y.-J. *ACS Appl. Mater. Interfaces* **2012**, *4*, 4752−4757.
(3) Wang, X.; Wu, X.-L.; Guo, Y.-G.; Zhong, Y.; Cao, X.; Ma, Y.; Yao, J. *Adv. Funct. Mater.* **2010**, *20*, 1680−1686.
(4) Liu, L.; Li, Y.; Yuan, S.; Ge, M.; Ren, M.; Sun, C.; Zhou, Z. *J. Phys. Chem. C* **2009**, *114*, 251−255.
(5) Cao, A.-M.; Hu, J.-S.; Liang, H.-P.; Wan, L.-J. *Angew. Chem., Int. Ed.* **2005**, *44*, 4391−4395.
(6) Guan, X.; Li, L.; Li, G.; Fu, Z.; Zheng, J.; Yan, T. *J. Alloys Comp.* **2011**, *509*, 3367−3374.
(7) Fang, D.; Li, L.; Xu, W.; Li, G.; Li, G.; Wang, N.; Luo, Z.; Xu, J.; Liu, L.; Huang, C.; Liang, C.; Ji, Y. *J. Mater. Chem. A* **2013**, *1*, 13203−13208.
(8) Sun, Z.; Kim, J. H.; Zhao, Y.; Bijarbooneh, F.; Malgras, V.; Lee, Y.; Kang, Y.-M.; Dou, S. X. *J. Am. Chem. Soc.* **2011**, *133*, 19314−19317.
(9) Chen, J. S.; Liang, Y. N.; Li, Y.; Yan, Q.; Hu, X. *ACS Appl. Mater. Interfaces* **2013**, *5*, 9998−10003.
(10) Bruce, P. G.; Scrosati, B.; Tarascon, J.-M. *Angew. Chem., Int. Ed.* **2008**, *47*, 2930−2946.
(11) Jeong, G.; Kim, Y.-U.; Kim, H.; Kim, Y.-J.; Sohn, H.-J. *Energy Environ. Sci.* **2011**, *4*, 1986.
(12) Tarascon, J. M.; Armand, M. *Nature* **2001**, *414*, 359−367.
(13) Poizot, P.; Laruelle, S.; Grugeon, S.; Dupont, L.; Tarascon, J. M. *Nature* **2000**, *407*, 496−499.
(14) Reddy, M. V.; Subba Rao, G. V.; Chowdari, B. V. *Chem. Rev.* **2013**, *113*, 5364−457.
(15) Reddy, M. V.; Beichen, Z.; Nicholette, L. J. e.; Kaimeng, Z.; Chowdari, B. V. R. *Electrochem. Solid-State Lett.* **2011**, *14*, A79−A82.
(16) Reddy, M. V.; Beichen, Z.; Loh, K. P.; Chowdari, B. V. R. *CrystEngComm* **2013**, *15*, 3568−3574.
(17) Li, J.; Xiong, S.; Li, X.; Qian, Y. *Nanoscale* **2013**, *5*, 2045−2054.
(18) Li, L.; Cheah, Y.; Ko, Y.; Teh, P.; Wee, G.; Wong, C.; Peng, S.; Srinivasan, M. *J. Mater. Chem. A* **2013**, *1*, 10935−10941.
(19) Reddy, M. V.; Yu, C.; Jiahuan, F.; Loh, K. P.; Chowdari, B. V. R. *RSC Adv.* **2012**, *2*, 9619−9625.
(20) Reddy, M. V.; Kenrick, K. Y. H.; Wei, T. Y.; Chong, G. Y.; Leong, G. H.; Chowdari, B. V. R. *J. Electrochem. Soc.* **2011**, *158*, A1423.
(21) Hu, L.; Qu, B.; Li, C.; Chen, Y.; Mei, L.; Lei, D.; Chen, L.; Li, Q.; Wang, T. *J. Mater. Chem. A* **2013**, *1*, 5596−5602.
(22) Xie, Q.; Li, F.; Guo, H.; Wang, L.; Chen, Y.; Yue, G.; Peng, D.-L. *ACS Appl. Mater. Interfaces* **2013**, *5*, 5508−5517.
(23) Hu, L.; Zhong, H.; Zheng, X. R.; Huang, Y. M.; Zhang, P.; Chen, Q. W. *Sci. Rep.* **2012**, *2*, 986.
(24) Zhou, L.; Zhao, D.; Lou, X. W. *Adv. Mater.* **2012**, *24*, 745−748.
(25) Zhang, G.; Yu, L.; Wu, H. B.; Hoster, H. E.; Lou, X. W. *Adv. Mater.* **2012**, *24*, 4609−4613.
(26) Ying, W.; Dawei, S.; Alison, U.; Jung-ho, A.; Guoxiu, W. *Nanotechnology* **2012**, *23*, 055402.
(27) Cherian, C. T.; Sundaramurthy, J.; Reddy, M. V.; Suresh Kumar, P.; Mani, K.; Pliszka, D.; Sow, C. H.; Ramakrishna, S.; Chowdari, B. V. R. *ACS Appl. Mater. Interfaces* **2013**, *5*, 9957−9963.
(28) Xing, Z.; Ju, Z.; Yang, J.; Xu, H.; Qian, Y. *Nano Res.* **2012**, *5*, 477−485.
(29) Weixin, Z.; Cheng, W.; Xiaoming, Z.; Yi, X.; Yitai, Q. *Solid State Ionics* **1999**, *117*, 331−335.
(30) Li, W.-N.; Zhang, L.; Sithambaram, S.; Yuan, J.; Shen, X.-F.; Aindow, M.; Suib, S. L. *J. Phys. Chem. C* **2007**, *111*, 14694−14697.
(31) Dong, Y.; He, K.; Yin, L.; Zhang, A. *Nanotechnology* **2007**, *18*, 435602.
(32) Fu, C.; Li, G.; Zhao, M.; Yang, L.; Zheng, J.; Li, L. *Inorg. Chem.* **2012**, *51*, 5869−5880.
(33) Munakata, F.; Takahashi, H.; Akimune, Y.; Shichi, Y.; Tanimura, M.; Inoue, Y.; Itti, R.; Koyama, Y. *Phys. Rev. B* **1997**, *56*, 979−982.
(34) Wakisaka, Y.; Hirata, S.; Mizokawa, T.; Suzuki, Y.; Miyazaki, Y.; Kajitani, T. *Phys. Rev. B* **2008**, *78*, 235107.
(35) Yu, C.; Guan, X.; Li, G.; Zheng, J.; Li, L. *Scripta Mater.* **2012**, *66*, 300−303.
(36) Langell, M. A.; Anderson, M. D.; Carson, G. A.; Peng, L.; Smith, S. *Phys. Rev. B* **1999**, *59*, 4791−4798.
(37) Dedryvère, R.; Laruelle, S.; Grugeon, S.; Poizot, P.; Gonbeau, D.; Tarascon, J. M. *Chem. Mater.* **2004**, *16*, 1056−1061.
(38) Varghese, B.; Teo, C. H.; Zhu, Y.; Reddy, M. V.; Chowdari, B. V. R.; Wee, A. T. S.; Tan, V. B. C.; Lim, C. T.; Sow, C. H. *Adv. Funct. Mater.* **2007**, *17*, 1932−1939.
(39) Wu, Z.-S.; Ren, W.; Wen, L.; Gao, L.; Zhao, J.; Chen, Z.; Zhou, G.; Li, F.; Cheng, H.-M. *ACS Nano* **2010**, *4*, 3187−3194.
(40) Cheng, K.; Yang, F.; Wang, G.; Yin, J.; Cao, D. *J. Mater. Chem. A* **2013**, *1*, 1669−1676.
(41) Beale, A. M.; Sankar, G.; Catlow, C. R.; Anderson, P. A.; Green, T. L. *Phys. Chem. Chem. Phys.* **2005**, *7*, 1856−60.
(42) Kruk, M.; Jaroniec, M. *Chem. Mater.* **2001**, *13*, 3169−3183.
(43) Smith, G. P.; Boston, C. R. *J. Chem. Phys.* **1961**, *34*, 1396−1406.
(44) Sun, X.; Qiu, X.; Li, L.; Li, G. *Inorg. Chem.* **2008**, *47*, 4146−4152.
(45) Tang, C.; Li, G.; Li, L. *Chem. Lett.* **2008**, *37*, 1138−1139.
(46) Fanning, J. C. *Coord. Chem. Rev.* **2000**, *199*, 159−179.
(47) Yu, L.; Zhang, L.; Wu, H. B.; Zhang, G.; Lou, X. W. *Energy Environ. Sci.* **2013**, *6*, 2664−2671.
(48) Reddy, M. V.; Wei Wen, B. L.; Loh, K. P.; Chowdari, B. V. R. *ACS Appl. Mater. Interfaces* **2013**, *5*, 7777−7785.
(49) Reddy, M. V.; Yu, C.; Jiahuan, F.; Loh, K. P.; Chowdari, B. V. R. *ACS Appl. Mater. Interfaces* **2013**, *5*, 4361−4366.

(50) Reddy, M. V.; Andreea, L. Y. T.; Ling, A. Y.; Hwee, J. N. C.; Lin, C. A.; Admas, S.; Loh, K. P.; Mathe, M. K.; Ozoemena, K. I.; Chowdari, B. V. R. *Electrochim. Acta* **2013**, *106*, 143−148.
(51) Courtel, F. M.; Duncan, H.; Abu-Lebdeh, Y.; Davidson, I. J. *J. Mater. Chem.* **2011**, *21*, 10206−10218.
(52) Laruelle, S.; Grugeon, S.; Poizot, P.; Dollé, M.; Dupont, L.; Tarascon, J.-M. *J. Electrochem. Soc.* **2002**, *149*, A627−A634.
(53) Li, X.; Qiao, L.; Li, D.; Wang, X.; Xie, W.; He, D. *J. Mater. Chem. A* **2013**, *1*, 6400−6466.
(54) Luo, D.; Li, G.; Guan, X.; Yu, C.; Zheng, J.; Zhang, X.; Li, L. *J. Mater. Chem. A* **2013**, *1*, 1220−1227.
(55) Luo, D.; Li, G.; Yu, C.; Yang, S. l.; Zheng, J.; Guan, X.; Li, L. *J. Mater. Chem.* **2012**, *22*, 22233−22241.
(56) Zhang, X.; Luo, D.; Li, G.; Zheng, J.; Yu, C.; Guan, X.; Fu, C.; Huang, X.; Li, L. *J. Mater. Chem. A* **2013**, *1*, 9721−9729.
(57) Fu, C.; Li, G.; Luo, D.; Zheng, J.; Li, L. *J. Mater. Chem. A* **2014**, *2*, 1471−1483.
(58) Reddy, M. V.; Subba Rao, G. V.; Chowdari, B. V. R. *J. Mater. Chem.* **2011**, *21*, 10003−10011.
(59) Reddy, M. V.; Madhavi, S.; Subba Rao, G. V.; Chowdari, B. V. R. *J. Power Sources* **2006**, *162*, 1312−1321.